Engineered Science
DOI: https://dx.doi.org/10.30919/es1459

Variable Speed Leakage Characteristics of Scroll Compressors for Miniature Compressed Energy Storage

Shijia Qi,[1, 2] Zhen Liu,[1, 2,*] Zheng Li,[1, 2] Zhichao Zhang[3] and Tengjun Huang[1, 2]

Abstract

Scroll compressor is especially suitable for miniature compressed air energy storage systems. The scroll compressors feature small size, low noise, lightweight, long service life, and high reliability. To investigate the evolution characteristics of transient flow fields in working chambers under variable rotational speeds, a three-dimensional transient model was established, and the dynamic grid technology was utilized to simulate the internal flow. The findings indicate that as the rotational speed increases, the leakage losses diminish, and the volumetric efficiency increases by 1.98% as the speed increases from 1200 to 3000 revolution per minute (RPM). During one working cycle, only the pressure in the exhaust chamber increases with increasing speed. Additionally, the temperature distribution is not even within the same compression chamber, with high-temperature regions concentrated in the region closer to the next high-pressure chamber.

Keywords: Variable rotational speed; Scroll compressor; Leakage characteristics; Numerical modelling.
Received: 10 January 2025; Revised: 21 February 2025; Accepted: 14 March 2025.
Article type: Research article.

1. Introduction

As an energy storage technology, compressed air energy storage, with its advantages of large storage capacity, long service life, and relatively low investment, has attracted significant attention in the energy field, including micro-compressed air energy storage systems.[1-5] Scroll compressors feature high efficiency, low vibration, low noise, and high reliability, making them the key energy conversion unit of the micro-compressed air energy storage system.[6-8] Rotational speed is a crucial parameter that significantly impacts the leakage of scroll compressors and their overall performance. Fu *et al*.[9] conducted comprehensive analyses of the influence of rotational speed on the scroll compressor performance, *e.g.*, friction loss, leakage loss, and flow loss of the scroll compressor using empirical formulas, but cannot reflect its effect on the detailed flow characteristics and their evolution in a dynamic process.

Cuevas *et al*.[10,11] modeled and experimentally tested an inverter scroll compressor, focusing on illustrating the variation rule of the scroll compressor operating performance with rotational speed in a certain speed range. Li *et al*.[12] analyzed the heat transfer process of variable-capacity compressors, established a mathematical model for thermal calculation, and obtained the influence of rotational speed on exhaust volume, volumetric efficiency, and leakage through programming. Meanwhile, the chamber leakage time and radial clearance change at different speeds. Cha *et al*.[13] established a simplified mathematical model of scroll compressor clearance leakage considering friction and adiabatic steady-state flow of compressible gases, etc., and analyzed the flow situation in the leakage clearance by using computational fluid dynamics (CFD).

Chen *et al*.[14] summarized the advantages and disadvantages of various leakage models comprehensively and put forward future research ideas for the scroll compressor leakage model. Liu *et al*.[15] reproduced the whole compression process of the scroll compressor, including suction, compression, and discharge, through numerical modeling, providing support for the optimal design of the compressor

[1] *Hubei Key Laboratory of Power System Design and Test for Electrical Vehicle, Hubei University of Arts and Science, Xiangyang, 441053, China*
[2] *School of Automotive and Traffic Engineering, Hubei University of Arts and Science, Xiangyang, 441053, China*
[3] *Department of Mechanical and Construction Engineering, Northumbria University, Newcastle upon Tyne, NE1 8ST, United Kingdom*
**Email:* liuzhen@hbuas.edu.cn (Z. Liu)

geometric structure. Liu *et al*.[16] conducted three-dimensional unsteady state numerical modeling of the flow characteristics in the working chamber, providing support for the structural design of the scroll compressor. Fang *et al*.[17] conducted an experimental study to investigate the performance characteristics of scroll compressors under various rotational speeds. Li *et al*.[18] examined the flow characteristics during pre-compression phenomena specifically in the suction process under variable-speed conditions, revealing that an increase in rotational speed leads to a reduction in the initial angle of pre-compression.

The research primarily focuses on analyzing the performance parameters and flow field characteristics of scroll compressors during their working process through experiments or mathematical thermal models. To investigate the evolution characteristics of transient flow fields in working chambers intuitively, this study employs dynamic mesh technology to examine the fluid flow process within scroll compressor chambers at various rotational speeds. The analysis focuses on the variations of the transient flow field within each chamber during one working cycle under various rotational speeds, as well as the impact of rotational speed on compression performance and leakage characteristics.

2. Mathematical model

2.1 Geometric parameter

The oil-free scroll compressor has two scroll teeth with the same profile but a 180° phase angle difference. The two teeth interact when the scroll compressor operates, with a certain distance between their centrals. One scroll is fixed, whilst the other one orbits against it. The basic geometric parameters are shown in Table 1.

The working chambers are formed by the engagement of the scroll teeth, as shown in Fig. 1. The dynamic rotation of the scroll disc causes changes in the volume of the working chamber, thereby enabling the intake, compression, and discharge of gas, which completes an entire working cycle.

2.2 Thermodynamic model

During one cycle, the pressure and temperature have the following relations Eqs. (1) and (2):

$$\frac{dP}{d\theta} = \left(\frac{\partial P}{\partial T}\right)_v \frac{dT}{d\theta} + \left(\frac{\partial P}{\partial v}\right)\frac{dv}{d\theta} \tag{1}$$

$$\frac{dT}{dt} = \frac{1}{mC_v}\left[\left(-T\left(\frac{\partial P}{\partial T}\right)_v\right)\left[\frac{dV}{dt} - v\Delta m\right] - \sum \dot{m}_{in}\,\Delta h + \dot{Q}\right] \tag{2}$$

where Δm is the mass difference, Δh is enthalpy difference, $\dot{Q}$ is heat transfer, T is the temperature of the air in the working chamber, P is the pressure of the medium in the working chamber, m is the mass of the air in the chamber, θ is the crank angle, C_v is the constant mass heat capacity of the air in the chamber, v is the specific volume of the air in the chamber. There is a radial clearance between the walls of the teeth engaged. The radial clearance occurs, on the one hand, because of the tolerance of machining or assembly and stress deformation during the working process, *etc.*, on the other hand, due to the need for a certain clearance between the wall surfaces of the scroll teeth during the scroll compressor work. Tangential leakage occurs as the gas flows through the radial clearance. Due to the pressure difference, the air in the high-pressure chamber flows into the low-pressure chamber through the radial clearance, resulting in tangential air leakage when the dynamic disc moves, as shown in Fig. 2(a). Meanwhile, there is an axial clearance between the top surfaces of the teeth and the bottom surfaces of the two discs, which is minimized using sealing gaskets. The airflow through the axial clearance is defined as radial leakage. In this model, the axial clearance is not considered.

Table 1: Geometric parameters of scroll compressor.

Parameter	Value
Base circle radius (mm)	3.675
Eccentric distance (mm)	5.745
Scroll teeth height (mm)	36
Scroll tooth thickness (mm)	5.8
Involute occurrence angle (rad)	0.789
Involute termination angle (πrad)	8.49

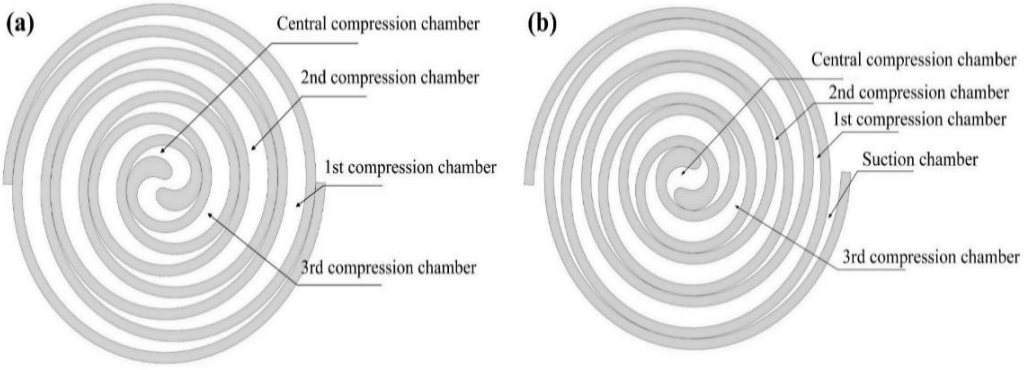

Fig. 1: Compressor chambers at a crank angle of (a) 0° and (b) 60°.

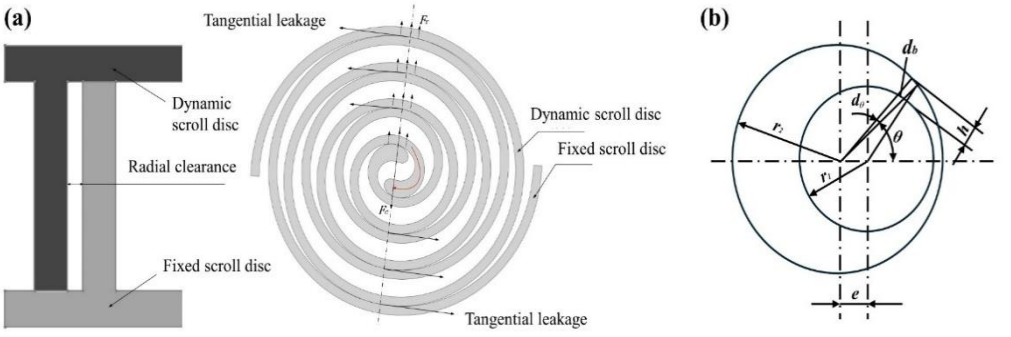

Fig. 2: (a) Tangential leakage model and (b) calculation model.

The dynamic scroll disc has a radial air force Eq. (3):

$$F_r = 2ah(P_1 - P_{i+1}) \tag{3}$$

where a is the basic circle radius of the scroll disc, h is the height of the scroll teeth, P_1 is the air pressure in the central compression chamber, andP_{i+1} is the air pressure in the first compression chamber.

Centrifugal inertia force in the rotation of a dynamic scroll disc Eq. (4):

$$F_c = m_r r_b \frac{\pi^2 n^2}{900} \tag{4}$$

where m_r is the unbalanced mass of the dynamic scroll disc against the central rotation, unbalanced mass because the dynamic scroll plate of the mass central axis and its rotational axis do not coincide, and r_b is the eccentricity of the dynamic scroll disc.

Generally, at any moment, under the combined effect of the radial air force and centrifugal inertia force, the clearance changes continuously. At the engaged clearance, the tangential leakage can be simplified as the flow between two eccentric annular clearances having different radii with eccentricity e, as shown in Fig. 2 (b). In Fig. 2 (b), r_1 and r_2 are their radii respectively. Since the actual clearance is very tiny, d_b is approximated as the distance between the two parallel flat discs, and the height h of the leakage clearance at an arbitrary angle θ is varied and can be expressed as Eq. (5):[19]

$$h \approx h_0 - e\cos\theta = h_0(1 - \varepsilon\cos\theta) \tag{5}$$

where h_0 is the clearance in the radius direction when the two circles are concentric, and ε is the relative eccentricity: $\varepsilon = e/h_0$.

The air is viewed as ideal air and tangential leakage can be determined by the following equation Eq. (6):[20]

$$\frac{dm_r}{d\theta} = \frac{\alpha_r \rho_i(\theta) c_r h_r}{\omega}\left\{\frac{2k}{k-1}RT_i(\theta) \times \left\{1 - \left[\frac{P_{i+1}(\theta)}{P_i(\theta)}\right]^{\frac{k-1}{k}}\right\}\right\}^{1/2} \tag{6}$$

where α_r is the flow coefficient, $\rho_i(\theta)$ is the density of the air in the i compression chamber at θ angle, h_r is the enthalpy, k is the multivariate index, $T_i(\theta)$ and $P_i(\theta)$ are the temperature and pressure of the air in the compression chamber at θ angle, respectively, and R is the air constant.

2.3 Model governing equations

The Reynolds time-averaged N-S equation to predict the mass, momentum, and energy conservation of the airflow are depicted in Eqs. (7-9), respectively.

$$\frac{\partial \rho}{\partial t} + \frac{\partial(\rho u_i)}{\partial x_i} = 0 \tag{7}$$

$$\frac{\partial(\rho u_i)}{\partial t} + \frac{\partial(\rho u_i u_j)}{\partial x_j} = \frac{\partial}{\partial x_j}\left(\mu \frac{\partial u_i}{\partial x_j}\right) - \frac{\partial p}{\partial x_j} \tag{8}$$

$$\frac{\partial T}{\partial t} + \frac{\partial(\rho u_j T)}{\partial x_j} = \frac{\partial}{\partial x_i}\left(\frac{\lambda}{c_p}\frac{\partial T}{\partial x_j}\right) + S_r \tag{9}$$

where ρ is the fluid density, u_i is the velocity in x, y, and z, x_i represents the coordinate component along the i-direction, μ is the dynamic viscosity coefficient, p is pressure, c_p is specific heat capacity, λ is heat conductivity, T is temperature, and S_r is the heat source.

3. Numerical research

3.1 Mesh

3.1.1 Mesh division

The scroll disc fluid domain is meshed using a geometric equirectangular adaptive binomial tree algorithm, which generates a highly adaptive binomial tree Cartesian mesh. Layering the fluid domain with normal isometric curves, the motion is automatically resized by continuously splitting the mesh to fit the geometric surface near the geometric boundaries. At the working position, different layers of the fluid domain have different orbital motion laws, whilst the points within the same layer have the same orbital motion law. The formation mesh is orthogonal, which has advantages such

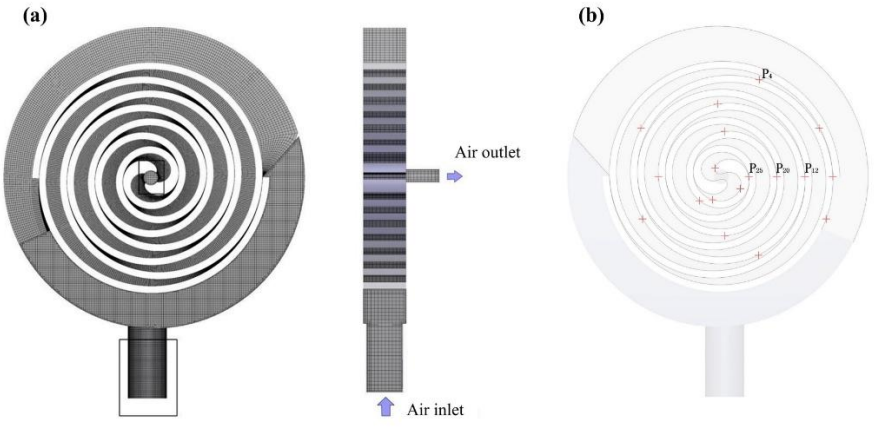

Fig. 3: Fluid field grid and monitoring point layout of layout scroll compressor at 0° crank angle (a) Grid division and (b) Monitoring point layout.

as small mesh deformation and small tilt. Kinematic regions with different numbers of meshes can be obtained by adjusting the number of division layers. The radial clearance and the chamber are meshed as the same domain, while the other regions are meshed separately using different fluid domains. The mesh is shown in Fig. 3(a). To obtain detailed information on the flow field, some monitoring points were set up as shown in Fig. 3(b).

3.1.2 Grid-independent verification

As shown in Fig. 4, the average outlet mass flow rate fluctuates slightly as the number of grids increases but the deviation remains within 0.2%. The number of grids has little effect on the calculation results within a certain grid range. Therefore, the number of grids 618,672 is selected (738,181 nodes), as a tradeoff between accuracy and computational costs.

3.2 Model validation

The model is validated against the data from the literature,[21] which is the model of oil-free air scroll compressor with a rated displacement of 84.0 cm^3/rev, a pressure ratio of 4.0, and a value of radial clearance of 0.04 mm. In the literature, the structural parameters of the scroll compressor are shown in Table 2, and the shear stress transport k-ω turbulence model was used. Fig. 5 shows the volumetric efficiency obtained from the simulation of this paper compared to the data in the literature. The results indicated that the maximum deviation between the simulation in this paper and the literature simulation results was 2.92% on volumetric efficiency. For the

Table 2: Geometric parameters of scroll compressor in the literature.

Parameter	Value
Base circle radius (mm)	2.77
Eccentric distance (mm)	4.71
Scroll teeth height (mm)	23.3
Scroll tooth thickness (mm)	4.0
Involute occurrence angle (rad)	0.72
Pitch of scroll involute (mm)	17.4
Radial clearance (μm)	40

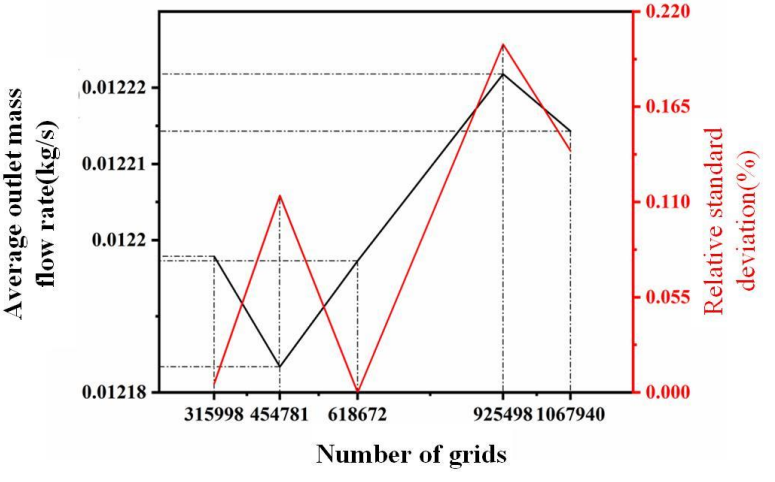

Fig. 4: Grid independence verification.

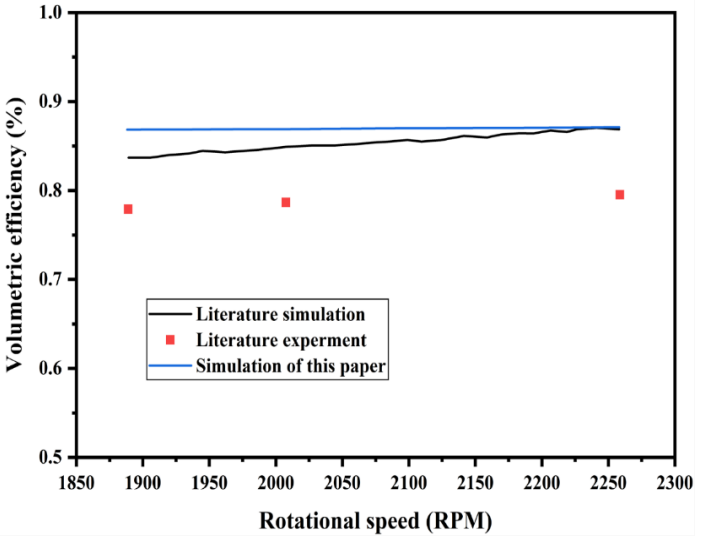

Fig. 5: Results of experiment and simulation.

actual scroll compressor, radial leakage remains possible even with a seal in place. Hence, the simulated volumetric efficiency will be slightly higher than the test results, with a maximum deviation of 6.89%. The deviation is reasonable, and it can be thought that the simulation result satisfies the actual requirement.

3.3 Boundary conditions and model setup

Assuming that there is no clearance in the axial direction and the radial clearance is 0.03 mm, the model is run at a transient state as the dynamic scroll disc moves. The Renormalization Group k-ε turbulence model is selected since strong turbulence is generated in the chambers. All walls are specified to be adiabatic, as the time of the entire process is too short for heat exchange between the air and the environment. Variable speed operating conditions are shown in Table 3.

4. Results and discussion

The flow field in the working chamber becomes stable after three cycles, with the mass flow rate at the inlet and outlet measured. Therefore, the fifth cycle is selected to observe the changes in the pressure, temperature, and velocity fields of the corresponding chambers in variable-speed cases. Here, a cycle consists of three processes: suction, compression, and exhaust.

4.1 Vent flow cross-sectional area and chamber volume

Fig. 6 shows the vent flow cross-section area versus the crank angle. It illustrates that the vent flow cross-sectional area of the central compression chamber increases gradually from 0° to 45° and then remains stable at 90 mm² until 135°, at which point the exhaust hole is entirely open. There is no covering on the exhaust hole by the dynamic scroll tooth head, thus maintaining the unchanged vent flow cross-section. After that, the area drops to its minimum value at 270° , where the volumes of the central compression chamber and the 3rd compression chamber are reduced to nearly zero and about 0.000025 m^3, respectively, as shown in Fig. 7.

The vent flow cross-section starts to increase after 270° until the next cycle, while the third compression chamber and the central compression chamber continue to decrease in volume until 300°. At this point, they merge and the exhaust hole opens to discharge air. In comparison, the volume of the 1st and 2nd compression chambers drops linearly throughout the entire cycle, whereas that of the suction chamber continues to increase, except for a slight drop after 315° .

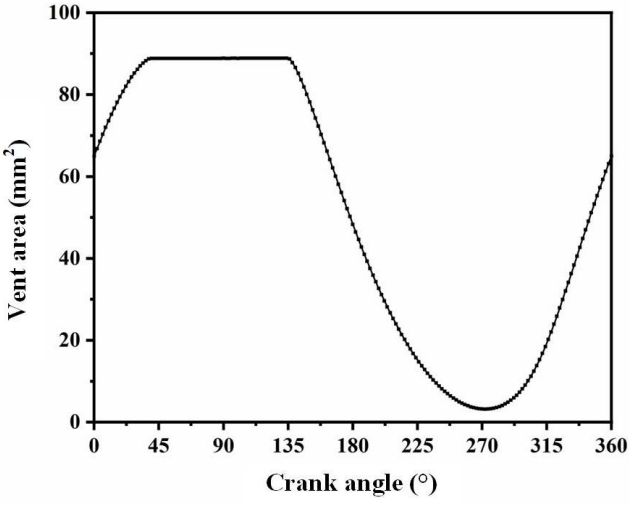

Fig. 6: Vent flow cross-sectional area versus crank angle.

Table 3: Variable speed operating condition.

Working condition	Rotation speed n/(RPM)	Inlet pressure P_s/Pa	Outlet pressure P_o/Pa	Inlet temperature T_s/K
1	1200	101320	607920	300
2	1800	101320	607920	300
3	2400	101320	607920	300
4	3000	101320	607920	300
5	3600	101320	607920	300
6	4200	101320	607920	300

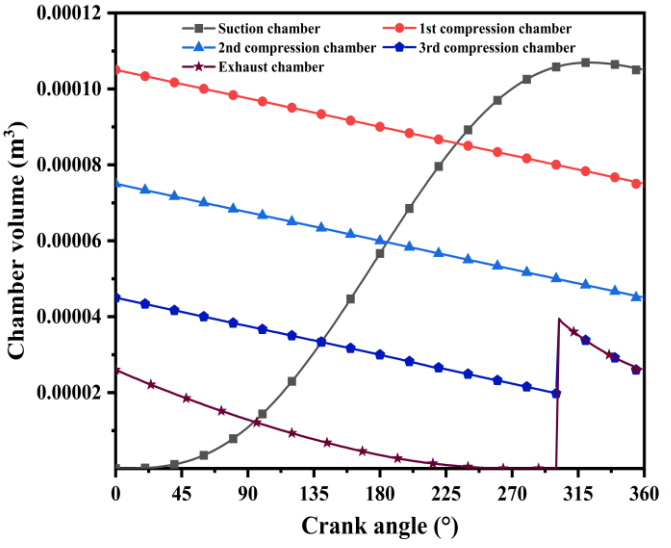

Fig. 7: Each compression chamber volume versus angle.

4.2 Velocity field

Fig. 8 shows the air velocity in the working chamber at different speeds and 0° crank angle. At this moment, the air suction was just completed, and the airflow rate becomes the main factor affecting pressure distribution in compression chambers. At each speed, the magnitude of velocity decreases gradually from the suction chamber to the center due to the lower pressure difference as the pressure in adjacent chambers increases. As the speed increases, the overall flow velocity magnitude becomes higher, which is attributed to faster suction and compression resulting from the increased rotation. Moreover, some regions near the marker point P12, P20, and P25 experience high air velocity (Fig. 8), regardless of rotation speeds, which is caused by leakage through radial clearances between chambers.

Since Fig. 8 indicates no visible leakage at P4, the plots in Fig. 9(a) have no significant spike. This is because P4 is in the suction chamber, where the pressure is not significantly different from that in the adjacent chamber. In contrast, at the very early phase, the plots in Figs. 9(b-d) all exhibit a spike that is over 10 times higher than their flat values, illustrating substantial leakage at P12, P20, and P25. At all marker points, the air velocity is always higher at increased speeds because the pressure difference at the three locations is much higher when the air flows from the high-pressure chamber to the low-pressure chamber, as shown in Fig. 13. Figs. 9(b-d) also illustrate that the flow velocity is reduced from P12 to P25, as a result of increased pressure and decreased pressure difference in the chambers close to the central compression chamber.

4.3 Mass flow

At all speeds, the inlet flow rates exhibit a very similar pattern, characterized by a peak of 0.022 kg/s at the early phase (approximately 45°), followed by several small fluctuations and a gradual rise at the end of the suction, as shown in Fig. 10(a). The peaks in these plots illustrate the suction process of the compressor, where the suction chamber opens and the air flows in. The following fluctuations indicate that the air is

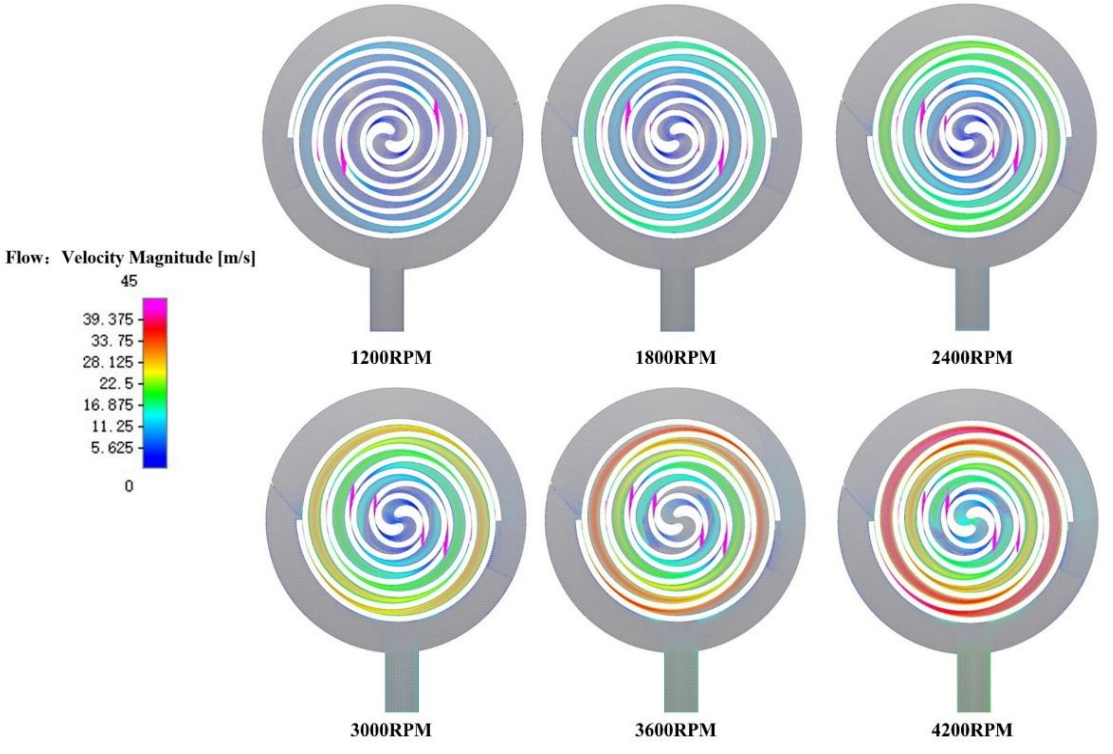

Fig. 8: Distribution of air velocity magnitude at different rotational speeds (θ =0).

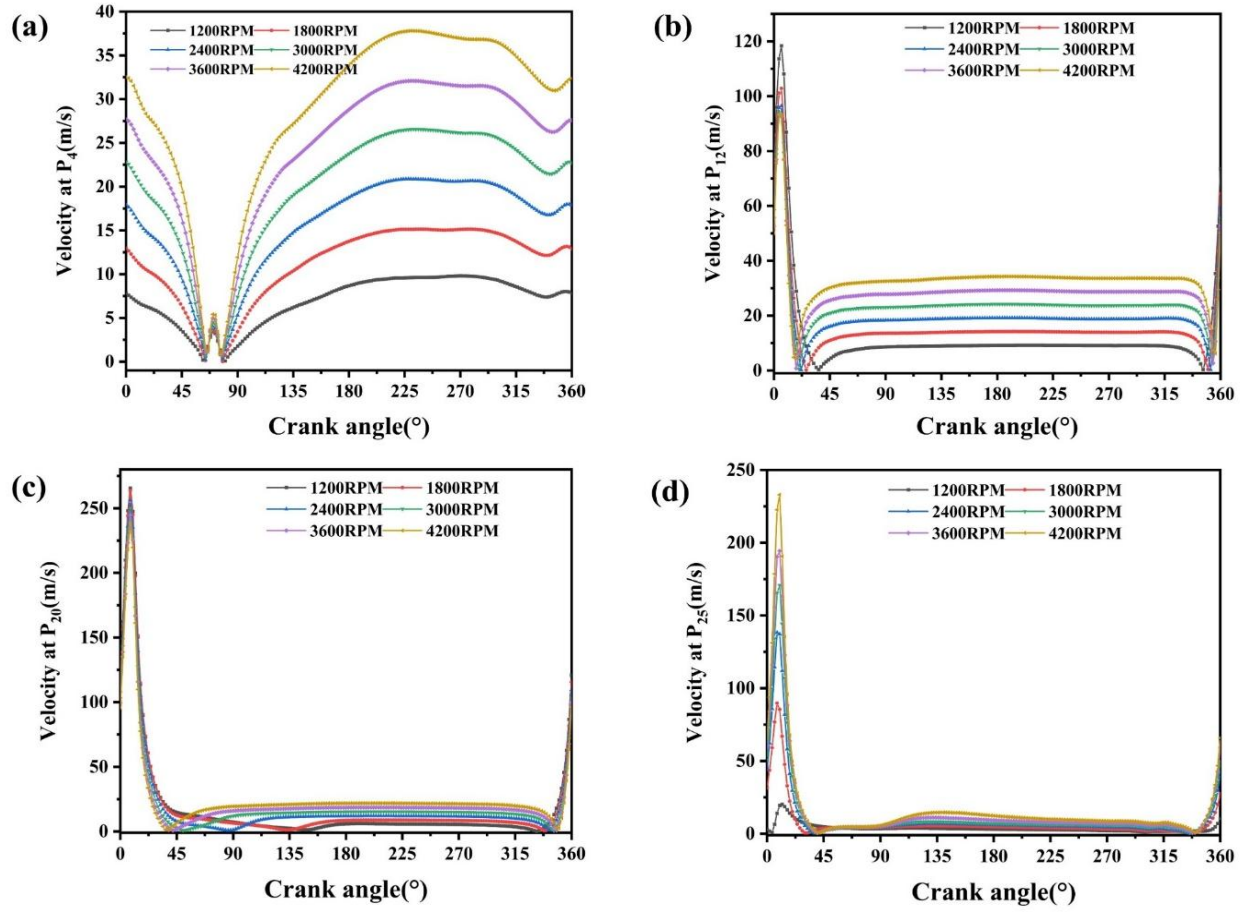

Fig. 9: Dynamic response curve of air velocity at marker points per unit crank angle (a) Velocity at P_4, (b) Velocity at P_{12}, (c) Velocity at P_{20}, and (d) Velocity at P_{25}.

flowing into the downstream compression chambers. Within the same compression chamber, the region closer to the next high-pressure chamber is defined as the downstream side and the region nearer to the low-pressure chamber is designated as the upstream side. Moreover, the inlet flow rate increases at higher speeds, primarily due to the stronger suction effect.

The inlet mass flow rate at each crank angle degree is shown in Fig. 10(b). At all speeds, the inlet flow rates exhibit very similar patterns, illustrating that they increase gradually from 0° to 25°, followed by a wave-like descent until 315°, and then rise. It also illustrates the short wave period at high (revolution per minute) RPMs, which means the airflow is fast .

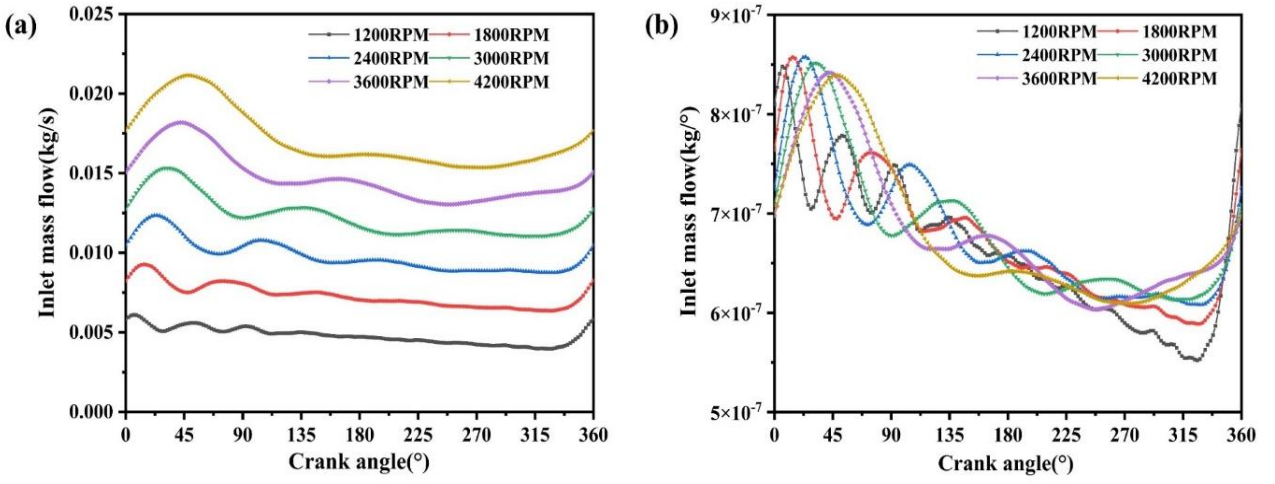

Fig. 10: The variable inlet mass flow rates of the scroll compressor at different speeds (a) Fluctuations and a gradual rise at the suction (b) The inlet mass flow rate at each crank angle degree.

Fig. 11 illustrates the outlet mass flow rate at all speeds, which has a similar pattern to Fig. 10(a), except that the peaks occur at the end of the exhaust process (between 315° and about 330°). The peaks indicate that the compressed air in the central compression chamber is being exhausted, with a flow rate that can be up to six times higher than the flow rate before the exhaust pipe opens. This is because, at 0-270° crank angle, the vent flow cross-section gradually increases, allowing the air to be largely discharged in a short time. The outlet mass flow rate initially increases after reaching its peak, then gradually reduces as the air is largely discharged. It is also shown that higher speed experiences a higher flow rate, which could be due to the higher exhaust efficiency.

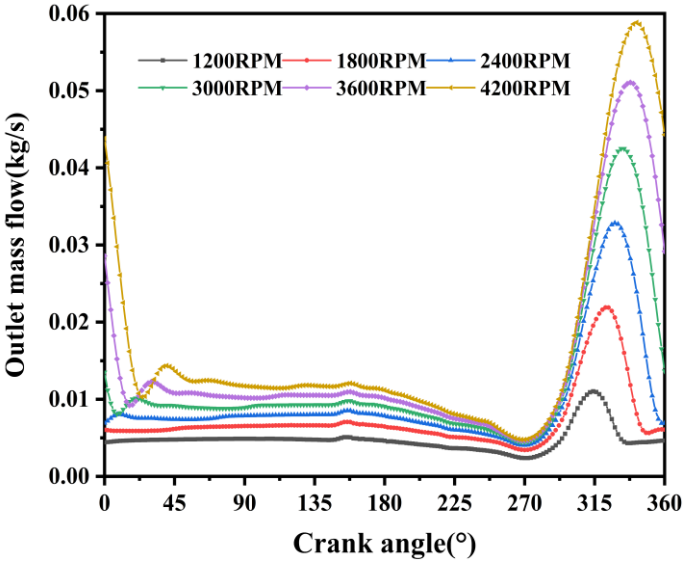

Fig. 11: Outlet mass flow with unit crank angle.

Fig. 12 is the average inlet and outlet mass flow rate with unit crank angle. Speed has a significant influence on the inlet and outlet mass flow rate. At higher speeds, more air flows into the suction chamber, making it more efficient. The changes in inlet and outlet average mass under unit crank angle show that: both inlet and outlet average mass flow rates increase with increasing speed, and it is linear; there is no air backflow at the outlet, affected by the tangential leakage airflow, the inlet and outlet average mass flow rate has a marked difference, the inlet average mass flow rate is slightly higher than that at the outlet, and with the increase in rotational speed, the leakage air volume is expanding progressively but is lower than that of suction air.

4.4 Pressure field

The pressure of the air in the working chamber at different speeds and 0° crank angle is shown in Fig. 13, where the suction camber has wholly disappeared, and the central compression chamber is connected to the exhaust hole. For all speeds higher than 1200 RPM, the pressure increases from the first compression chamber to the central chamber and reaches its maximum in the center, resulting from the multi-stage compression.

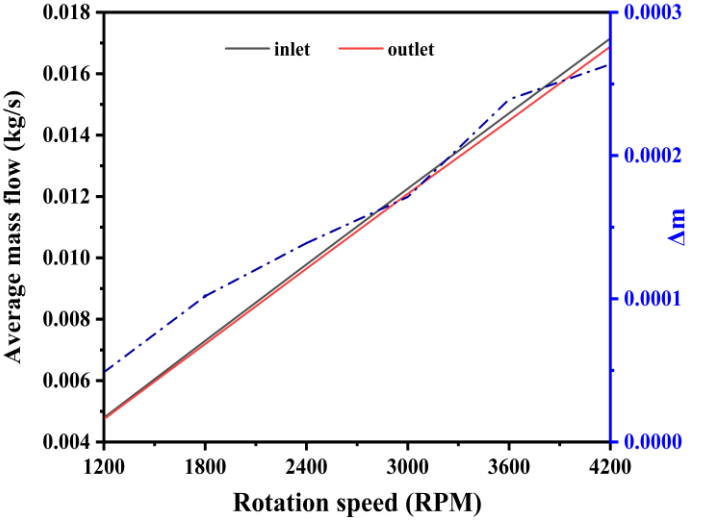

Fig. 12: Average inlet and outlet mass flow rate with unit crank angle.

Moreover, the pressure difference between adjacent chambers is pronounced. When the speed increases from 1800 to 4200 RPM, the pressure in the 3rd compression chamber drops due to higher airflow speeds. Meanwhile, the pressure in the exhaust chamber increases at higher speeds because its volume changes more rapidly, while the amount of air discharged is limited by the size of the exhaust pipe. The pressure in the suction chamber, the 1st and 2nd compression chambers, drops slightly when the speed rises, which is not visible in the contours.

Fig. 14 shows the compression chamber pressure as a function of crank angle, ranging from 0 to 1440°. It described the pressure in each chamber in a complete working cycle. The air enters the suction chamber at crank angles from 0° to 360°, and then the 1st, 2nd, and 3rd compression chambers, after another 360°, respectively. It illustrates that the pressure in the suction chamber drops dramatically and fluctuates during the early phase, before about 90°, and then gradually returns to atmospheric pressure by the end of the suction. The reasons are twofold: on one hand, when the crank starts to move, the inlet mass flow rate grows rapidly (Fig. 10(b)) and the suction chamber volume increases (Fig. 7), and the air from the environment is sucked into the suction chamber very quickly via an inlet pipe, which causes turbulence; on the other hand, the air in the 1st compression chamber leaks into the suction chamber through the radial clearance further enhancing the

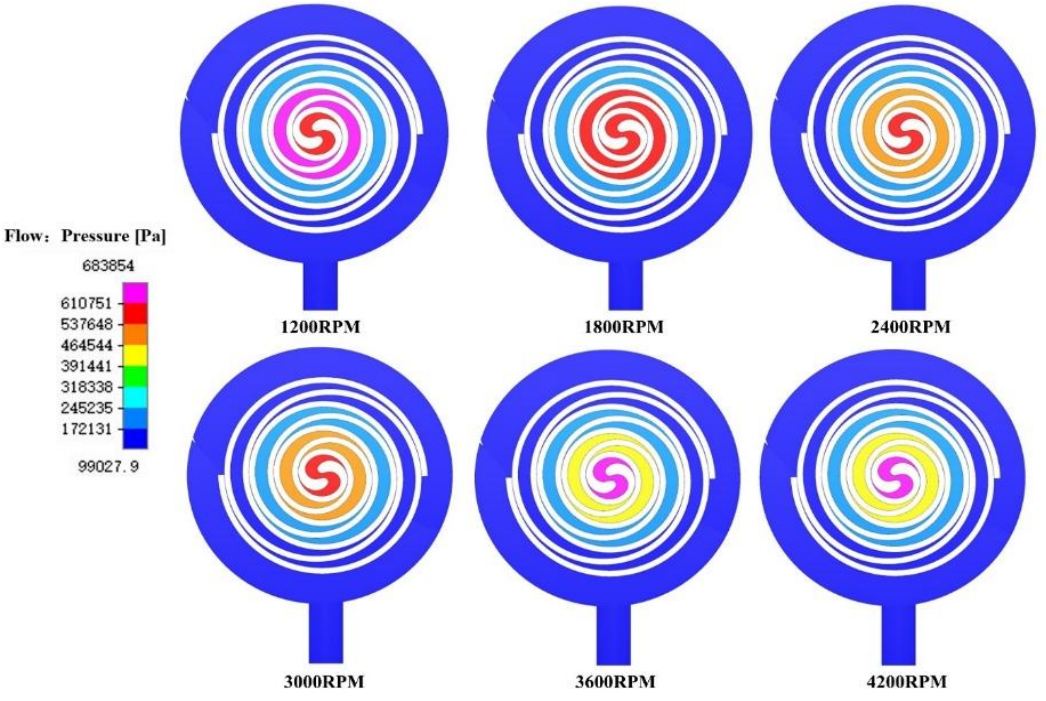

Fig. 13: Pressure contour at different speeds (θ =0º).

turbulence in the suction chamber.

After that initial phase of suction, the air pressure in the suction chamber varies slightly and is relatively close to atmospheric pressure. During the entire suction process, Fig. 14 also indicates that the pressure changes become significant with rotation speeds; that is, the higher the speed, the faster the airflow and the lower the pressure. However, the pressure in the suction chamber rises at the crank angle about from 300° to 360°, in this case, the inlet in the suction chamber gradually decreases until it is completely closed, where the volume change rate of the suction chamber is minor or even negative, and the air is pre-compressed, so the pressure is going up.

The pressure of the air keeps increasing in the 1st and 2nd compression chambers, and its values and rising rates are higher at lower speeds. It may be caused by the higher temperature in these chambers, due to a longer time for heat transfer and prolonged air leakage. So there is a high pressure at lower speeds. When the air enters the 3rd compression chamber at crank angle from 1080° to 1440°, its pressure continues to increase. Eventually, it reaches its peak before entering the central compression chamber and being exhausted. At about 1080-1350° crank angle, the slope of the line at lower RPM declines slowly. In comparison, the line at higher RPM rises rapidly in Fig. 14, indicating that the pressure-increasing rates at lower speeds are lower than those at higher speeds. Consequently, after around 1260°, the pressure at low RPM is lower than at high RPM.

The pressures reach their peak and then drop dramatically when the third compression chambers merge into the central compression chamber, and the exhaust hole opens to discharge air near 1380°, corresponding to Fig. 7. At approximately 300°, the curve of the third compression chamber coincides with the curve of the exhaust chamber. The peak may occur because the exhaust chamber volume is nearly zero at approximately 270° (Fig. 7), the vent flow cross-sectional area is close to zero (Fig. 6), and the pressure increases with increasing speed, resulting in higher pressure.

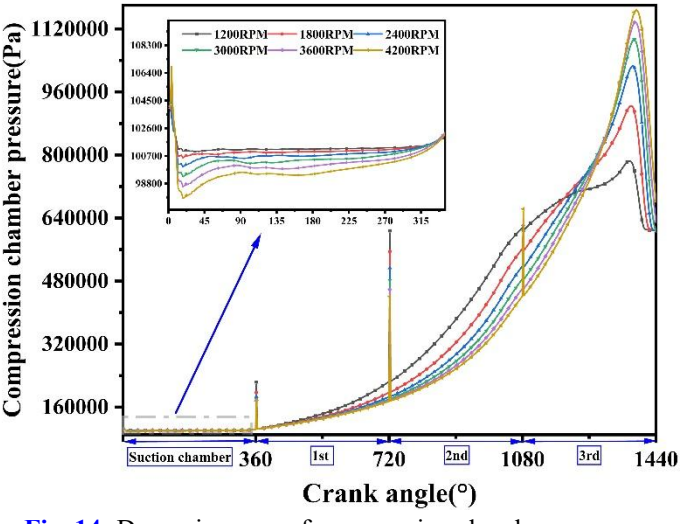

Fig. 14: Dynamic curve of compression chamber pressure.

4.5 Temperature field

Fig. 15 illustrates the temperature distribution in the scroll compressor at various speeds and a 0° crank angle. At each

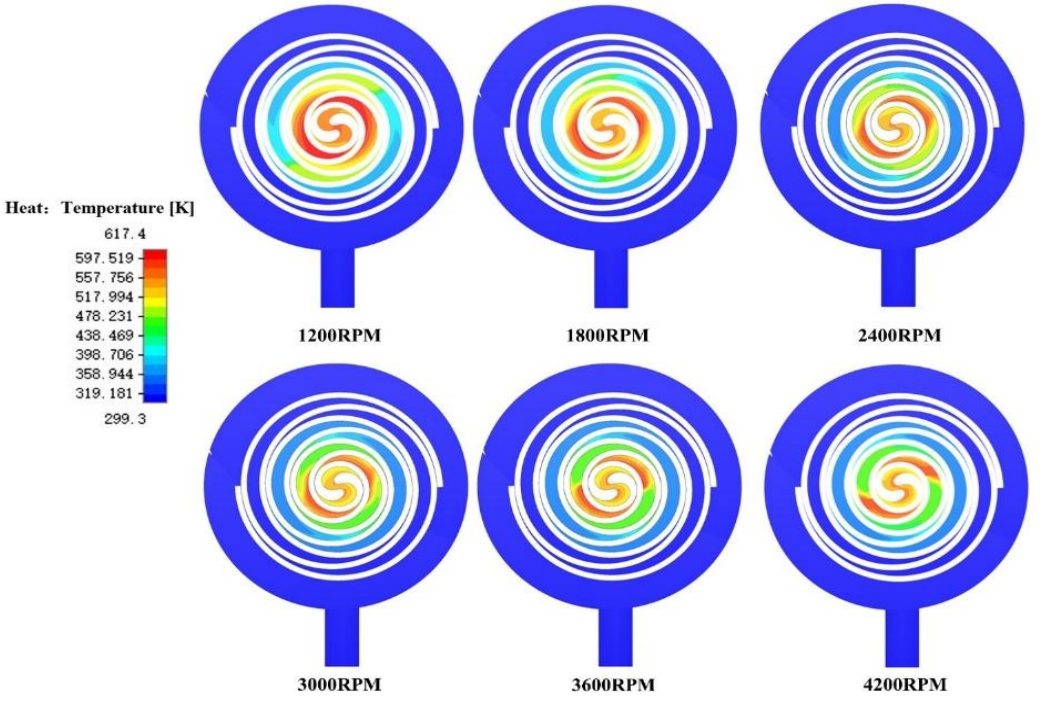

Fig. 15: Temperature distribution at different rotational speeds(θ =0°).

speed, similar to the pressure contour shown in Fig. 13, the temperature increases gradually from the suction chamber to the central compression chamber, as the compression process. When the rotational speed increases, the temperature in all chambers decreases. The reason may be that higher speeds result in insufficient time for heat transfer. From Fig. 15, it can also be seen that the temperature in the central compression chamber is lower than that in its adjacent chamber, which has the highest temperature.

For the rest chambers, the temperature increases as they approach the central compression chamber. In the same compression chamber, the temperature downstream is generally higher than that of the upstream (as shown in the 3rd compression chamber at 4200 RPM in Fig. 15). This is because the air leaked from the high-pressure chamber is mixed with the air flowing from upstream to downstream and thus forms the eddy, which disrupts the temperature in the low-pressure chamber. Moreover, the tangential leakage is severe at low speeds, resulting in increased frequency and time for air heat exchange in the chamber, and the air temperature diffuses noticeably upstream. On the other hand, the leaked air is repeatedly compressed in the low-pressure chamber, which contributes to the increase in air temperature.

Fig. 16 illustrates the change in outlet temperature at varying rotational speeds. At 0-270° crank angle, as the crank angle increases, the outlet temperature decreases at all speeds and reaches its minimum at approximately 100-160° due to the exhaust. At the early phase of exhaust, the temperature increases gradually within the central compression by the compression process until about 270°, followed by a slight drop when the exhaust chamber volume drops to nearly zero (Fig. 7). The temperature shortly increases to its peak value at about 315°, which might be caused by the leaked air. It then decreases until the air is exhausted substantially. During most periods of the exhaust (from 0° to about 270°), the temperature is lower at higher speed. Between about 270° and 315°, the temperature at higher speeds starts to exceed that at lower speeds.

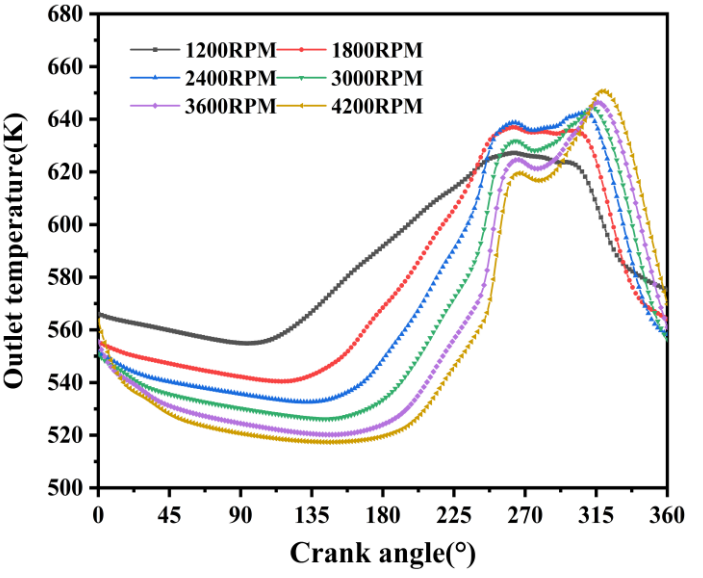

Fig. 16: Dynamic response curve of exhaust outlet total temperature per unit crank angle.

4.6 Volumetric flow

The volumetric flow rate is a critical parameter that characterizes the output performance of positive displacement compressors, as it reflects both the utilization rate of the working chambers and internal leakage. The theoretical volumetric flow rate of a scroll compressor can be expressed as Eq. (10):

$$q_{vth} = nV_s \tag{10}$$

The actual volume flow rate expression is shown in Eq. (11):

$$q_v = \eta_v q_{vth} \tag{11}$$

where n is the scroll compressor speed, η_v is the volumetric efficiency, and V_s is the scroll compressor suction chamber volume.

The volumetric efficiency is defined as the ratio of the actual volumetric flow rate to the theoretical volumetric flow rate. Fig. 17 illustrates the variation of volumetric efficiency with rotating speed. The volumetric efficiency exhibits a nonlinear increasing trend with rotating speed, characterized by a rapid increase in the low-speed range (1200-1800 RPM), followed by a plateau of 0.874 at 3000 RPM, and ultimately a gradual stabilization in the high-speed range (>3000 RPM). When the speed exceeds 3000 RPM, the volumetric efficiency decreases slightly due to flow restriction at the suction port, which prevents timely air intake into the suction chamber. The volumetric efficiency increased by 1.98% as the speed increased from 1200 RPM to 3000 RPM. The data indicate that the enhancement primarily occurred within the speed range of 1200-3000 RPM, suggesting that increasing speed has a pronounced effect on improving volumetric efficiency in the lower speed range.

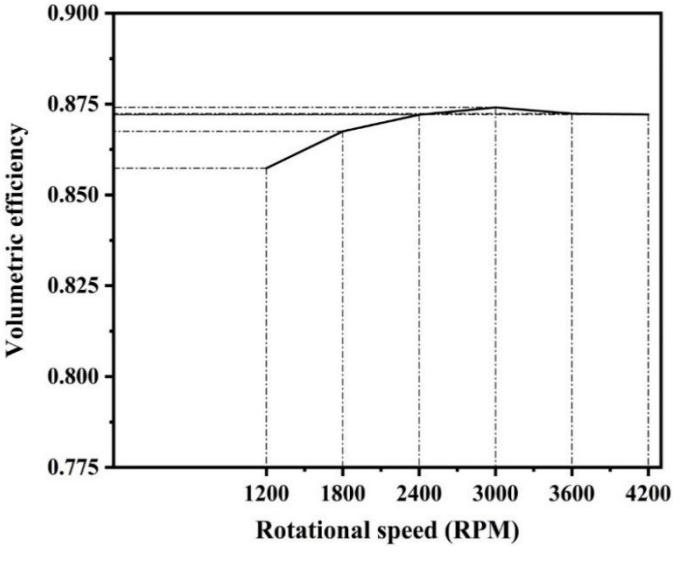

Fig. 17: Volumetric efficiency characteristic curve condition.

5. Conclusion

The main conclusions are as follows:

(1) Rotating speed significantly affects leakage, with leakage decreasing as RPM increases. At low rotational speeds, the scroll compressor is unable to generate sufficient air suction, leading to increased leakage and lower compression efficiency. The volumetric efficiency increases by 1.98% as speed increases from 1200 RPM to 3000 RPM.

(2) During one working cycle of the scroll compressor, the pressure variation in the suction chamber remains relatively small. Due to air leakage into the suction chamber during the suction process, a pre-compression phenomenon occurs when the crankshaft rotation angle ranges from 300° to 360°. The maximum pressure appears at the discharge outlet of the exhaust chamber, exceeding 11.2×10^5Pa and the pressure in the exhaust chamber increases with increasing speed.

(3) The temperature in each chamber decreases as the speed increases. At the same RPM, the temperature in the central compression chamber is lower than that in its adjacent chamber, which has the highest temperature. In the same compression chamber, the high-temperature region becomes increasingly concentrated in the region closer to the next high-pressure chamber due to leakage.

Acknowledgement

This work is supported by National Natural Science Foundation of China, Grant Nos. 52472405; Hubei Natural Science Foundation Innovation and Development Joint Fund Project, 2022CFD083; Hubei Superior and Distinctive Discipline Group of "New Energy Vehicle and Smart Transportation", XKTD022023; Key program of Xiangyang Technology project (High Tech Field), 2021ABH004233.

Conflict of Interest

There is no conflict of interest.

Supporting Information

Not applicable.

References

[1] Y. Kim, D. Favrat, Energy and exergy analysis of a micro-compressed air energy storage and air cycle heating and cooling system, *Energy*, 2010, **35**, 213-220, doi: 10.1016/j.energy.2009.09.011.

[2] A. Facci, D. Sánchez, E. Jannelli, S. Ubertini, Trigenerative micro compressed air energy storage: Concept and thermodynamic assessment, *Applied Energy*, 2015, **158**, 243-254, doi: 10.1016/j.apenergy.2015.08.026.

[3] Y. Xu, J. Fang, H. Zhang, S. Song, L. Tong, B. Peng, F. Yang,

Experimental investigation on the output performance of a micro compressed air energy storage system based on a scroll expander, *Renewable Energy*, 2025, **243**, 122602, doi: 10.1016/j.renene.2025.122602.

[4] H. Sun, X. Luo, J. Wang, Feasibility study of a hybrid wind turbine system–Integration with compressed air energy storage, *Applied Energy*, 2015, **137**, 617-628, doi: 10.1016/j.apenergy.2014.06.083.

[5] X. Zhang, C. Qin, Y. Xu, W. Li, X. Zhou, R. Li, Y. Huang, H. Chen, Integration of small-scale compressed air energy storage with wind generation for flexible household power supply, *Journal of Energy Storage*, 2021, **37**, 102430, doi: 10.1016/j.est.2021.102430.

[6] M. Cheayb, M. Marin Gallego, M. Tazerout, S. Poncet, Modelling and experimental validation of a small-scale trigenerative compressed air energy storage system, *Applied Energy*, 2019, **239**, 1371-1384, doi: 10.1016/j.apenergy.2019.01.222.

[7] C. Mohamad, M. G. Mylène, P. Sébastien, T. Mohand, Micro-scale trigenerative compressed air energy storage system: modeling and parametric optimization study, *Journal of Energy Storage*, 2019, **26**, 100944, doi: 10.1016/j.est.2019.100944.

[8] B. Castellani, E. Morini, B. Nastasi, A. Nicolini, F. Rossi, Small-scale compressed air energy storage application for renewable energy integration in a listed building, *Energies*, 2018, **11**, 1921. doi: 10.3390/en11071921.

[9] L. Fu, Q. Li, R. Xu, Research on volumetric efficiency of compressor at variable speed in automobile air-conditioning, *Journal of Refrigeration*, 2008, **29**, 29-32, doi: 10.3969/j.issn.0253-4339.2008.02.006.

[10] C. Cuevas J. Lebrun, Testing and modelling of a variable speed scroll compressor, *Applied thermal engineering*, 2009, **29**, 469-478, doi: 10.1016/j.applthermaleng.2008.03.016.

[11] C. Cuevas, N. Fonseca, V. Lemort, Automotive electric scroll compressor: Testing and modeling, *International Journal of Refrigeration*, 2012, **35**, 841-849, doi: 10.1016/j.ijrefrig.2011.11.019.

[12] C. Li, G. Li, M. Zhao, X. Liu, Performance Prediction Model for Scroll Compressors with Variable Volume, *Chemical Engineering & Machinery*, 2016, **43**, 379-383, doi: 10.3969/j.issn.0254-6094.2016.03.023.

[13] H. Cha, Y. Song, J. Wang, Y. Jiang, X. Chou, A gas leakage model in the leakage clearance of scroll compressor, *Engineering Thermophysics*, 2016, **37**, 1438-1443.

[14] R. Chen, W. Wang, Discussion on leaking characters in meso-scroll compressor, *International Journal of Refrigeration*, 2009, **32**, 1433-1441, doi: 10.1016/j.ijrefrig.2009.02.009.

[15] S. Liu, X. Kang, C. Shan, Y. Hu, Numerical simulation of three-dimension unsteady flow in the compression chambers of a scroll compressor, Proceedings of 22nd International Compressor Engineering Conference at Purdue, July 14-17, 2014, 1-7.

[16] Z. Liu, Z. Li, D. Xie, H. Wu, Unsteady characteristic and flow mechanism of a scroll compressor in small-scale compressed air energy storage system, *Journal of Energy Storage*, 2022, **51**, 104368. doi: 10.1016/j.est.2022.104368.

[17] J. Fang, Y. Xu, H. Zhang, Z. Yang, J. Wan, Z. Liu, Experimental research on the output performance of scroll compressor for micro scale compressed air energy storage system, *Sustainability*, 2023, **15**, 15665, doi: 10.3390/su152115665.

[18] Z. Li, L. Liu, J. Wang, R. Hou, Z. Wang, D. Cui, Unsteady flow and thermal dynamic performance of pre-compression characteristics in variable-speed scroll compressors, *Applied Thermal Engineering*, 2024, **257**, 124327, doi: 10.1016/j.applthermaleng.2024.124327.

[19] Z. Li, Z. Liu, H. Wu, D. Xie, W. Qian, Tangential leakage transient flow field characteristics of scroll compressor, *Energy Storage Science and Technology*, 2021, **10**, 1579-1588, doi: 10.19799/j.cnki.2095-4239.2021.0176.

[20] H. Mahfouz, M. Hassan, and M. Musa, Analytical and experimental study on a scroll compressor, International Conference on Compressors and Refrigeration at Purdue, July 12-15, 2004, 1-11.

[21] Q. Zhang, J. Feng, J. Wen, X. Peng, 3D transient CFD modelling of a scroll-type hydrogen pump used in FCVs, *International Journal of Hydrogen Energy*, 2018, **43**, 19231-19241, doi: 10.1016/j.ijhydene.2018.08.158.